THE JOURNAL OF PHYSICAL CHEMISTRY C

Article

pubs.acs.org/JPCC

Ag Dewetting in Cu@Ag Monodisperse Core−Shell Nanoparticles

Anya Muzikansky, Pilkhaz Nanikashvili, Judith Grinblat, and David Zitoun*

Department of Chemistry, Bar Ilan Institute of Nanotechnology and Advanced Materials (BINA), Bar Ilan University, Ramat Gan 52900, Israel

ABSTRACT: We report on the synthesis of monodisperse Cu and Cu@Ag nanocrystals. Using the same synthetic procedure in three different temperature ranges, Cu@Ag show very different stability pathways which we interpret as three different growth mechanisms: galvanic displacement at low temperature, metal assisted growth, and overgrowth of Ag at high temperature. At middle range temperature, Ag shell is shown to be stable over several months and efficiently passivates the Cu core. In the two other cases, combined dynamic light scattering (DLS) and high-resolution transmission electron microscopy (HRTEM) demonstrate the diffusion processes of Ag taking place at the surface of Cu and the dewetting of Ag shell from the surface of Cu to form spherical Ag nanocrystals. This result is a nice example of aging of core/shell nanostructure, and the chemical rearrangement is put in perspective of previously reported theoretical calculations and applications to printed electronics.

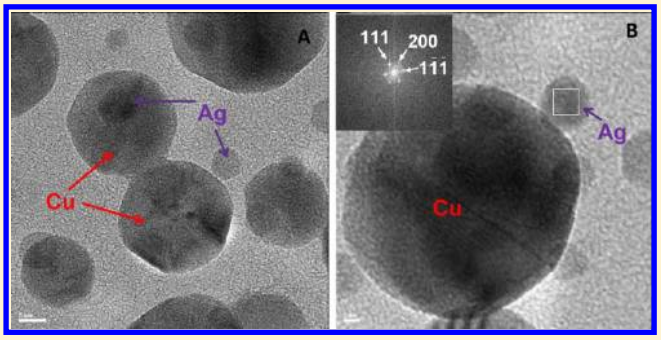

INTRODUCTION

Core−shell nanoparticles are usually forecast as promising building block for their optical properties and catalytic activities.[1,2] A variety of core−shell structures, including metal, oxide, semiconductor, and organic material, have been synthesized. In the case of metallic core−shell structure, most of the research has focused on noble metals with the keynote example of Au growth on nanocrystals of different shapes.[3] Galvanic displacement has yielded a vast catalogue of structures including core/shell, hollow particles (Kirkendall effect), and alloys depending on the kinetics of the mass transport.[4−6] From a technological point of view, core−shell structure allows the replacement of a noble expensive metal at the core of the particles by a cheaper one. Outer metallic shell passivates the inner metallic core and avoids side reactions, mainly oxidation. Colloidal inks, which have demonstrated their ability for the printing of current collector for solar cells, RFID tag, and even transparent conductive coatings, consist in Ag colloidal dispersions and could be advantageously replaced by a more affordable transition metal, in particular Cu. Syntheses of monodisperse core and core−shell nanoparticles have been explored by colloidal synthesis.[7,8] $Cu_{core}Ag_{shell}$ or Cu@Ag colloids have been synthesized to provide a passivation against oxidation of Cu. There are a few synthetic routes which yield Cu@Ag NPs, via physical vapor deposition,[9] redox-transmetalation method in aqueous solution,[10−12] and microwave-assisted polyol process.[13,14] Transmetalation consists in the galvanic displacement of the core metal by a second metal displaying a higher redox potential. This route is highly specific and self-limited since the nucleation of the second metal takes place only on the sacrificial core.[15]

In this article, we report on the synthesis of monodisperse Cu and Cu@Ag nanocrystals. We demonstrate the diffusion processes of Ag taking place at the surface of Cu. We do observe the dewetting of Ag shell from the surface of Cu to form spherical cluster by dynamic light scattering (DLS) and high-resolution transmission electron microscopy (HRTEM). Cu@Ag stability has also been demonstrated for a certain range of temperature growth of the shell. In these synthetic conditions, Ag shell is shown to be stable over several months and efficiently passivates the Cu core.

EXPERIMENTAL SECTION

Synthesis of Cu NPs. $Cu(acac)_2$ anhydrous (98%, STREM Chemicals), $AgNO_3$ (99.9%, STREM Chemicals), and oleylamine (90%, Fisher) were dried and kept in a dry atmosphere until use. Prior to use, all chemicals were flushed with nitrogen. $Cu(acac)_2$ (0.382 mmol, 0.1 g) and 10 mL of oleylamine (OAm) were added in a 100 mL three-necked flask. The flask was connected to the Schlenk line and flushed with nitrogen at room temperature. The solution was heated to 230 °C at 10 °C/min and was kept at this temperature for 3 h under continuous stirring under N_2. Eventually the red dark colloidal solution was cooled rapidly (quenching) using a water bath. The flask was moved to the glovebox. The dispersion was centrifuged three times at 10 000 rpm for 30 min to separate the solid product. Finally, the red dispersion was obtained by dispersing the dark solid in hexane.

Received: November 6, 2012
Revised: December 5, 2012
Published: December 5, 2012

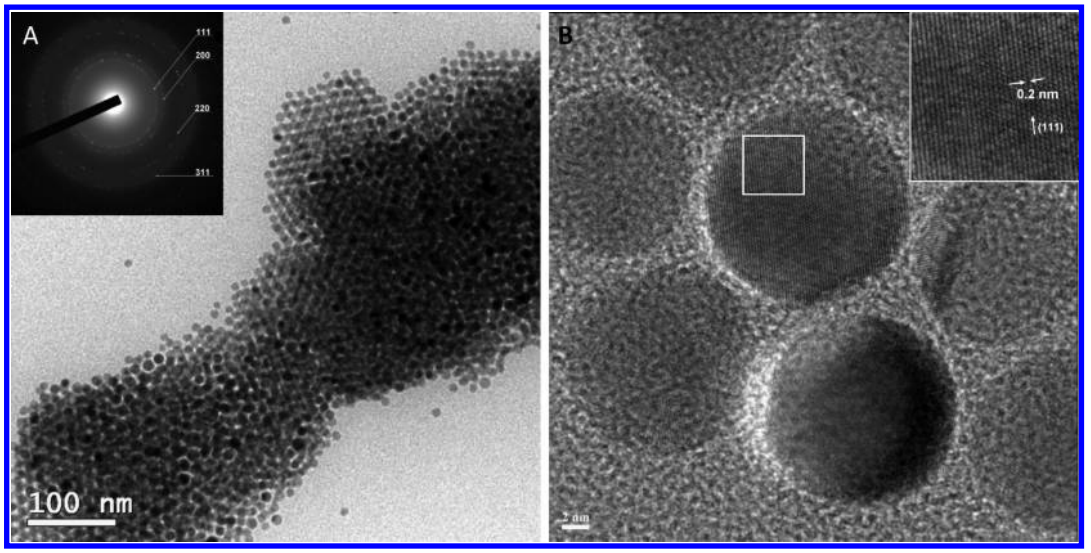

Figure 1. TEM pictures of Cu NPs with corresponding electron diffraction (inset) (A). HRTEM of single crystalline Cu NPs with lattice fringes along the (111) direction (B).

Synthesis of Cu@Ag NPs. Cu NPS were synthesized according to the protocol described above. $AgNO_3$ (0.096 mmol, 0.016 g for 4/1 atomic ratio between Cu and Ag) was mixed with 8 mL of oleylamine (OAm). The solution was then bubbled with N_2 for a few minutes and added dropwise over 2 min in the Cu NPs dispersion using a syringe. The dark solution was stirred overnight at room temperature under nitrogen. Depending on the synthesis, a further heating step at temperatures between 75 and 150 °C was performed for 2 h. Hexane was added, and the dispersion was centrifuged three times at 6000 rpm for 30 min to separate the solid product. Finally the blue/red dispersion was obtained by dispersing the dark solid in hexane.

Characterization. The NPs structure was investigated by transmission electron microscopes (TEM): FEI Tecnai-12 at 120 kV and JEOL JEM-2100 (LaB6) at 200 kV for high-resolution imaging (HRTEM). The HRTEM is integrated with a digital scanning device (STEM) comprising annular dark-field (DF) and bright-field (BF) detectors and with a Thermo Scientific energy-dispersive X-ray spectrometer (EDS) system for elemental analysis. The TEM observations were made by taking BF and DF images, HRTEM images, and selected area electron diffraction (SAED) patterns. Fourier transform analysis (FFT) of high-resolution images technique was used for structural analysis. Elemental analysis, scanning, and mapping were performed in STEM mode, and the elemental analysis was performed using the EDS system equipped with the Noran System Six software. Samples were prepared by placing a drop of diluted sample on a 400 mesh carbon-coated nickel grid. XRD measurement have been made on a Bruker AXS D8 advance, Cu Kα = 1.5418 Å radiation. Absorption spectra of the NPs colloidal dispersion were measured using a spectrophotometer Varian Cary 5000. Electron paramagnetic resonance has been collected on a Bruker X-band EMX spectrometer at T = 298 and 77 K.

Dynamic light scattering was measured on a Sympatek Nanophox instrument with a He−Ne laser (λ = 632.8 nm) based on photon cross-correlation spectroscopy (PCCS) in order to avoid multiple scattering. Scattering angle is set to 90° and temperature to 25 °C, and measurements were performed three times at two different concentrations. All hydrodynamic average diameter and polydispersity were calculated from the non-negative least-squares fitting of the autocorrelation curve using the Stokes−Einstein equation.

RESULTS

Cu NPs Synthesis. The thermal decomposition of $Cu(acac)_2$ in oleylamine (OAm) medium yields Cu NPs.[16] Two amine groups coordinate Cu(II) metal center to yield a blue complex. Above 200 °C, the solution turns red while OAm is presumably oxidized.[17] The large excess of OAm acts as a stabilizing agent. After purification and dispersion in hexane, the colloidal dispersion has been analyzed by TEM, HRTEM, DLS, and UV−vis spectroscopy. Electron diffraction (Figure 1a inset) shows that NPs crystallize in the FCC crystallographic structure of bulk Cu within the space group *Fm*-3*m* (JCPDS 04-0836, a = 3.615 Å). HRTEM (Figure 1b) shows single crystalline NPs, almost spherical without noticeable sign of oxide shell. The Cu NPs polydispersity is low according to the TEM analysis (D = 13.0 ± 2.0 nm), and they tend to self-assemble. The colloidal dispersion in hexane is stable for months in a glovebox. When exposed to air, the change in color from red to green is very slow in colloidal dispersion but faster if the sample is dried.

The NPs size distribution is confirmed by DLS measurement using the photon cross-correlation spectroscopy technique (Figure 7A). The hydrodynamic radius is found to be D_H = 14.1 ± 2.8 nm; a schematic view of Cu NPs surrounded with a single layer of extended OAm ligands bound through the amine groups would give a 1.8 nm layer and a theoretical value of 16.6 nm based on TEM size. The difference between the theoretical value and the experimental hydrodynamic diameter may be due to the disordered solvated amine layer, very different from a closed packed fully extended OAm layer. In the following, these Cu NPs serve as basis for the growth of Ag shell while we systematically measure the Cu NPs by DLS for each batch to ensure the reproducibility of the results.

Cu@Ag Synthesis by Galvanic Displacement. The growth of Ag shell is achieved by galvanic displacement of Cu by Ag(I). The silver source is an OAm complex of Ag(I) formed in situ by dissolving $AgNO_3$ in OAm. At room temperature, a controlled experiment has shown that no Ag is

dx.doi.org/10.1021/jp3109545 | J. Phys. Chem. C 2013, 117, 3093−3100

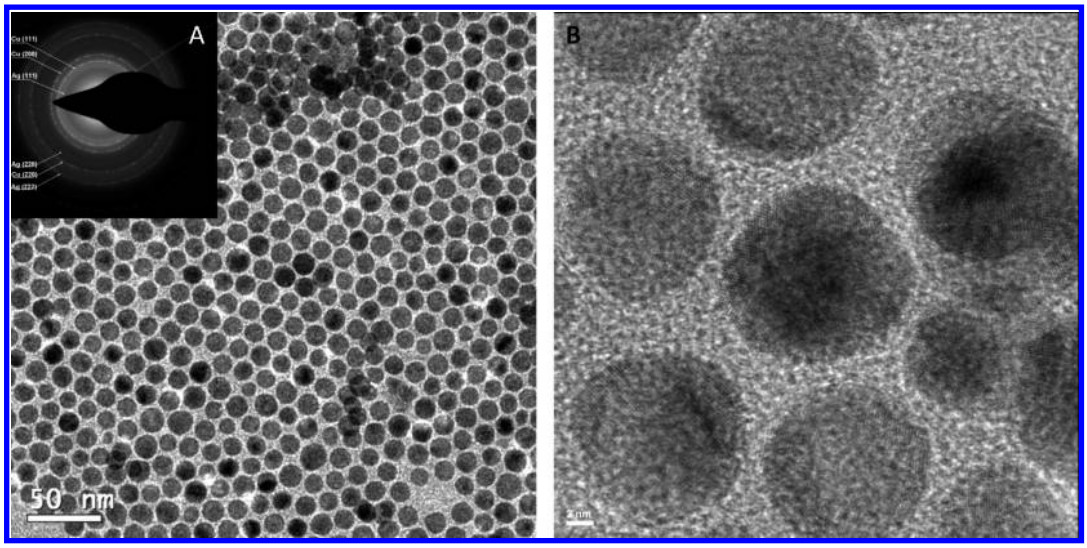

Figure 2. TEM pictures of Cu@Ag 4/1 ($Cu_4@Ag_1$; shell grown at T = 25 °C) NPs with selected area electron diffraction (inset) (A). HRTEM of polycrystalline $Cu_4@Ag_1$ NPs (B).

formed even with long reaction time. In fact, reduction of Ag^+ by oleylamine only occurs above 110 °C in the time scale of the experiment. The galvanic displacement yields Cu@Ag nanoparticles which are named according to the initial ratio used between the two metals (namely $Cu_8@Ag_1$, $Cu_4@Ag_1$, $Cu_1@Ag_1$, and $Cu_1@Ag_4$). In all synthetic procedures, the dispersion is stirred overnight at room temperature to ensure the complete coating of Cu NPs. Figure 2 shows a TEM picture of $Cu_4@Ag_1$ NPs self-assembly. Electron diffraction analysis of Cu@Ag shows the presence of crystalline Cu and poorly crystalline Ag. The very diffuse diffraction rings correspond to the {111}, {200}, and {220} crystal planes of face-centered cubic (fcc) Ag (JCPDS 04-0783, a = 4.090 Å). The diffraction rings correspond to face-centered cubic (fcc) Cu (JCPDS 04-0836, a = 3.615 Å). HRTEM (Figure 2B) shows polycrystalline NPs with some crystalline areas. The thinness of the shell, estimated to an atomic monolayer in average according to the Cu/Ag stoichiometry, prevents the complete characterization. The ratio between Cu and Ag has been measured by energy-dispersive X-ray spectroscopy (EDS) mounted on TEM and E-SEM. For $Cu_8@Ag_1$, $Cu_4@Ag_1$, $Cu_1@Ag_1$, and $Cu_1@Ag_4$, the atomic ratio is measured to be 7.62/1, 4.82/1, 5.55/1, and 3.58/1. The ratio saturates above a 4/1 initial ratio within the standard deviation error, which is typical of a self-limiting reaction while Ag atomic layer is completed. In the following we shall consider only two characteristic ratios 4/1 and 1/1.

Dark-field TEM (using {111} reflection of Ag) shows the mapping of Ag in the bimetallic NPs (Figure 3B). The resolution is not high enough to ascertain the formation of a complete shell, but the comparison with bright-field TEM image (Figure 3A) clearly indicates the nucleation of Ag only on Cu NPs and the bimetallic character of all the particles.

Galvanic Displacement Mechanism. Therefore, the most important question relies in the understanding of reaction mechanism and in visualizing how effective is the method to yield core/shell NPs. To answer these questions, we rely mainly on the EPR to demonstrate the mechanism and on XRD to demonstrate the core/shell structure. EPR is performed on solutions after filtration to remove the NPs at T = 298 and 77 K; the EPR bands are characteristic of Cu(II) complexes (quadruplet from hyperfine interaction of electron spin S = 1/2 with the Cu nuclear spin I = 3/2). After synthesis, we observe a very weak signal, probably from unreacted Cu(II) precursor (Figure 4A); the signal is much larger (2 orders of magnitude) after addition of Ag(I) in the solution and corresponds to the release of Cu(II) in solution. This experiment supports the galvanic displacement schema.

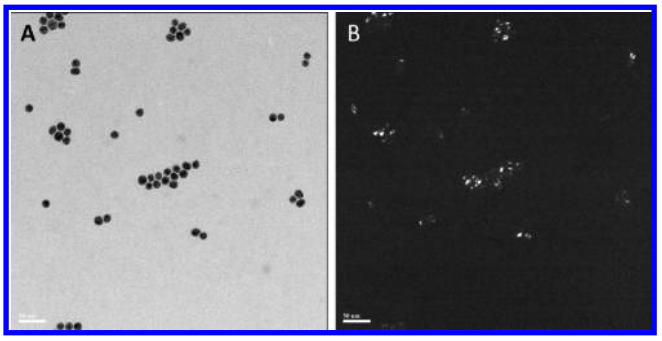

Figure 3. TEM pictures of $Cu_1@Ag_1$ NPs (shell grown at T = 25 °C) bright (A) and dark field (B).

The XRD is collected on the pristine sample and after 3 months on the same powder (Figure 4B). Interestingly, no sign of oxidation is observed. The XRD is consistent with a main phase of FCC Cu and a secondary phase of Ag (very broad [111] peak). The same measurement is conducted on Cu NPs powder sample; after 3 months, the copper is oxidized to Cu_2O and CuO (inset of Figure 4B).[18] The Ag layer is effectively protecting the Cu core from oxidation.

Aging of Cu@Ag Grown by Galvanic Displacement. Since aging has been done on a powder sample, the same is carried out on Cu@Ag colloidal dispersions. The dispersion is kept in a closed vial for several months in the dark; the red-blue color does not radically change, but TEM gives a surprising result (Figure 5). After 12 months, TEM reveals the formation of very small NPs (1−3 nm) surrounding the original 13 nm NPs. This effect has been observed for $Cu_4@Ag_1$ and $Cu_1@Ag_1$ colloidal samples when Ag shell is grown at room temperature. The dispersion is washed thoroughfully to ensure that Ag NPs do not arise from unreacted Ag(I) that could be reduced in the time span.

dx.doi.org/10.1021/jp3109545 | J. Phys. Chem. C 2013, 117, 3093−3100

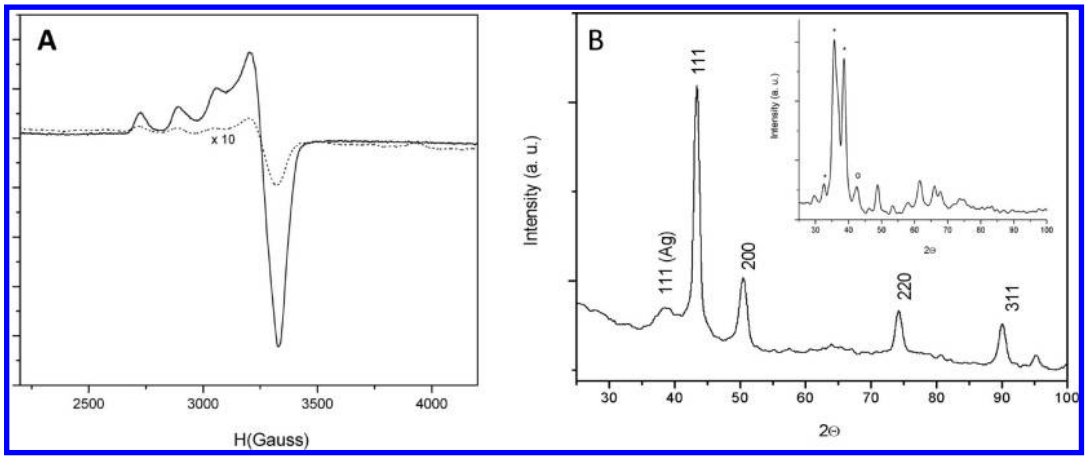

Figure 4. Electron paramagnetic resonance (EPR) at T = 77 K of the supernatant of a Cu NPs dispersion before (dotted line) and after (plain line) the addition of Ag^+ to the colloidal dispersion (A). XRD of the $Cu_4@Ag_1$ NPs powder exposed to air for 3 months (inset XRD of Cu NPs exposed to air for 3 months) (B).

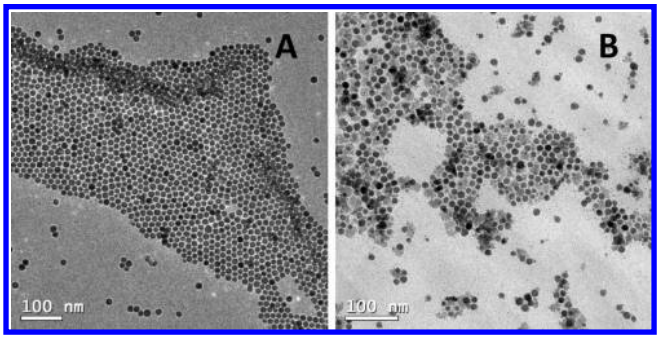

Figure 5. TEM pictures of $Cu_4@Ag_1$ NPs (shell grown at T = 25 °C) after synthesis (A). Colloidal dispersion aged for 12 months (B).

Overgrowth of Ag Shell and Aging. We believe that the stability of Ag shell could be improved by a temperature treatment after synthesis. In the synthesis, a heating step at T > 120 °C for 2 h is added after overnight galvanic displacement. In a controlled experiment, we observe the formation of 4 nm Ag NPs only above T = 120 °C, which stands as the experimental activation temperature for self Ag nucleation. When Ag shells are grown above 120 °C, TEM does not show any small Ag NPs right after synthesis of $Cu_4@Ag_1$ and $Cu_1@Ag_1$ (EDS gives an atomic ratio close to the theoretical stoichiometry (3.1:1 for $Cu_4@Ag_1$ and 1.3:1 for $Cu_1@Ag_1$). After 12 months aging, the same sample consists in Cu NPs (around 16 nm in size) and Ag NPs (2−4 nm in size) (Figure 6A,B). In this case, the formation of Ag is obviously not resulting from unreacted Ag(I) since the Ag shell has been grown at a temperature high enough for a complete reaction of Ag(I). In aged samples, Ag NPs are distributed on Cu NPs and are also free-standing.

Since electron microscopy does not provide a reliable statistics, the Ag shell stability has been studied directly in colloidal dispersions using dynamic light scattering. The samples dispersed in hexane are stable for months, and DLS have been collected systematically on samples for 12 months (Figure 7). The PCCS technique allows us to get reliable results even for very small NPs or polydisperse samples. The hydrodynamic radius has been calculated from the Stokes−Einstein equation using table parameters for the viscosity, density, and refractive indexes of hexane, Cu, and Ag.

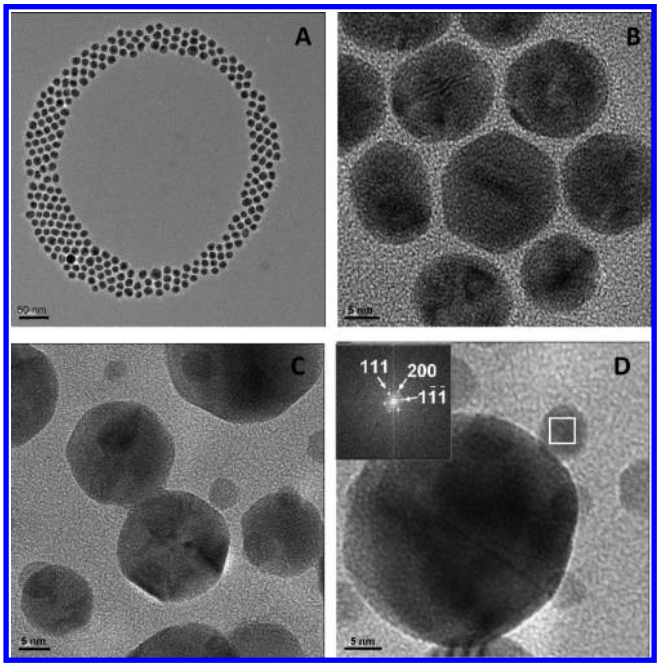

Figure 6. Cu_1Ag_1 NPs (shell grown at T = 150 °C): TEM and HRTEM pictures from a fresh colloidal dispersion (A) and (B) and from a colloidal dispersion aged during 12 months (C) and (D). Inset FFT of the white frame on the image (C).

In the case of Cu@Ag NPs, mean values are calculated from the stoichiometry measured by EDS. Cu NPs hydrodynamic radius is found to be 14.1 ± 2.8 nm (compared to 13.0 ± 2.0 nm from TEM); the difference accounts for a ligand shell of folded OAm, and this point is currently investigated in detail. When the Ag shell is grown by galvanic displacement, the increase in particle size is within the error bar ($Cu_4@Ag_1$ 13.9 ± 3.6 nm) with a slight increase in polydispersity. After 1 year, the size distribution obtained from DLS is bimodal 17.6 ± 3.8 and 1.3 ± 0.4 nm (Figure 7B). This aging affect is also observed when the shell is overgrown. DLS (Figure 7C) is performed on the $Cu_1@Ag_1$ shown in Figure 6 with the following size distributions for pristine, 3 months, and 1 year old samples: 15.0 ± 8.3 nm; 17.6 ± 3.8 and 1.2 ± 0.5 nm; 20.1 ± 15.5 and 3.1 ± 3.0 nm. Figure 7D shows the size distribution variation over a 12 month time span.

dx.doi.org/10.1021/jp3109545 | J. Phys. Chem. C 2013, 117, 3093−3100

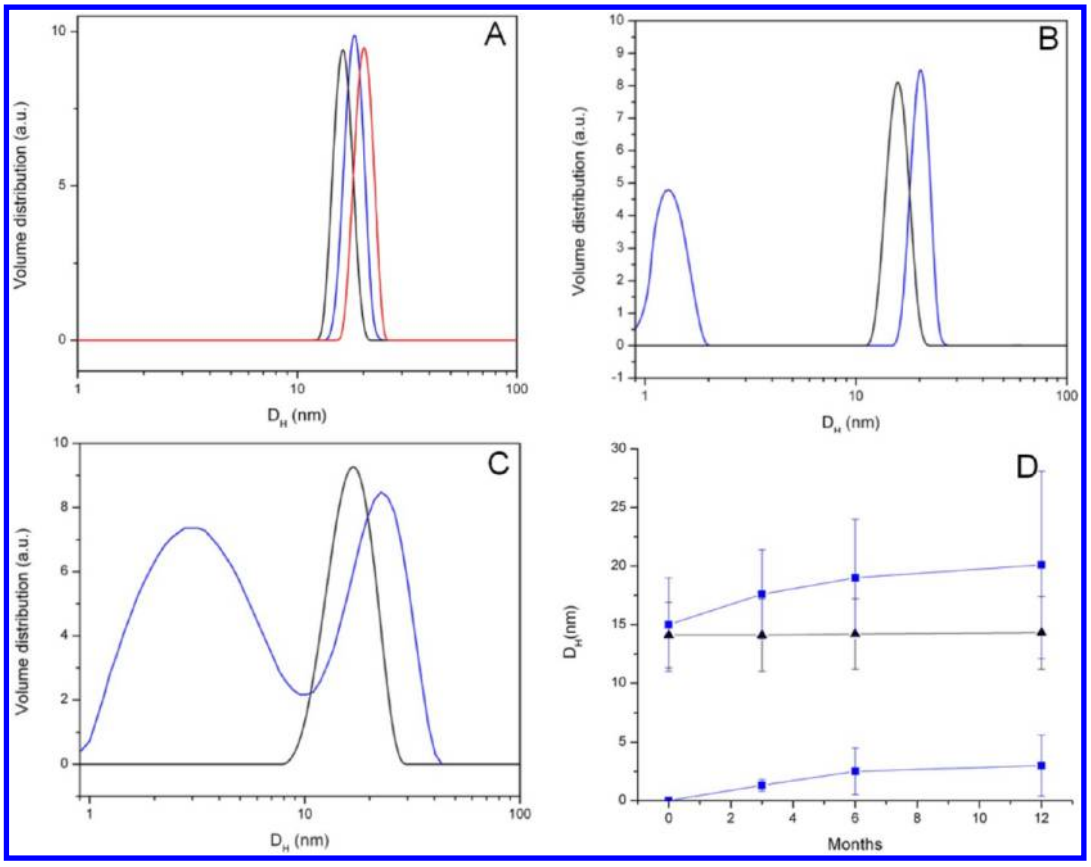

Figure 7. Size distribution calculated from dynamic light scattering of Cu (black), $Cu_4@Ag_1$ (blue), and $Cu_1@Ag_1$ (red) after 1 year aging (metal assisted nucleation) (A). Size distribution of $Cu_4@Ag_1$ by galvanic displacement: pristine (black) and after 1 year aging (blue) (B). Size distribution of $Cu_1@Ag_1$ by shell overgrowth: pristine (black) and after 1 year aging (blue) (C). Aging process on $Cu_4@Ag_1$ grown by metal assisted nucleation (black) and $Cu_1@Ag_1$ by shell overgrowth (blue) (D).

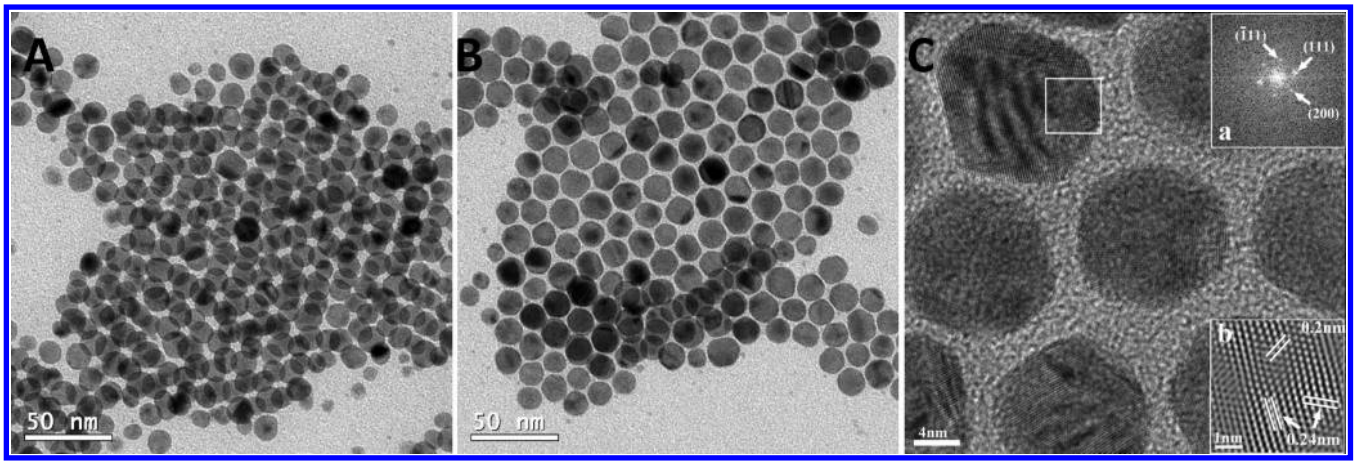

Figure 8. TEM pictures of $Cu_4@Ag_1$ NPs (metal assisted nucleation) after synthesis (A). $Cu_4@Ag_1$ colloidal dispersion aged during 1 year TEM (B) and HRTEM of $Cu_1@Ag_1$ (C). Inset FFT from the region marked with a white square (a), magnified and filtered image from the same area (b).

These results confirm the aging of Ag shell grown by galvanic displacement and by shell overgrowth, as already observed in TEM. A more quantitative analysis shows that the aging occurs in three steps: formation of Ag NPs on the surface of Cu, release of Ag NPs, and Ostwald ripening.

Metal Assisted Nucleation of Ag Shell and Aging. Ag shell is now grown at a moderate temperature below self-nucleation of Ag between 50 and 120 °C (typically T = 75 °C). DLS of Cu, $Cu_4@Ag_1$, and $Cu_1@Ag_1$ have been collected on samples for 12 months. Figure 7A shows the size distribution after 12 months: 14.1 ± 2.8 nm; 15.9 ± 3.3 and 17.5 ± 3.7 nm. The hydrodynamic diameter increases with Ag content, which demonstrates an effective growth of Ag shell, beyond the Ag monolayer deposited by galvanic displacement. EDS gives an atomic ratio close to the theoretical stoichiometry (3.1:1 for $Cu_4@Ag_1$ and 0.9:1 for $Cu_1@Ag_1$). On pristine samples or after 12 months, the size distribution is giving the exact same numbers (Figure 7D). TEM images show the sample $Cu_4@Ag_1$ after synthesis and 12 months later (Figure 8A,B); the particle size distribution from image analysis remains the same at 13.5

dx.doi.org/10.1021/jp3109545 | J. Phys. Chem. C 2013, 117, 3093−3100

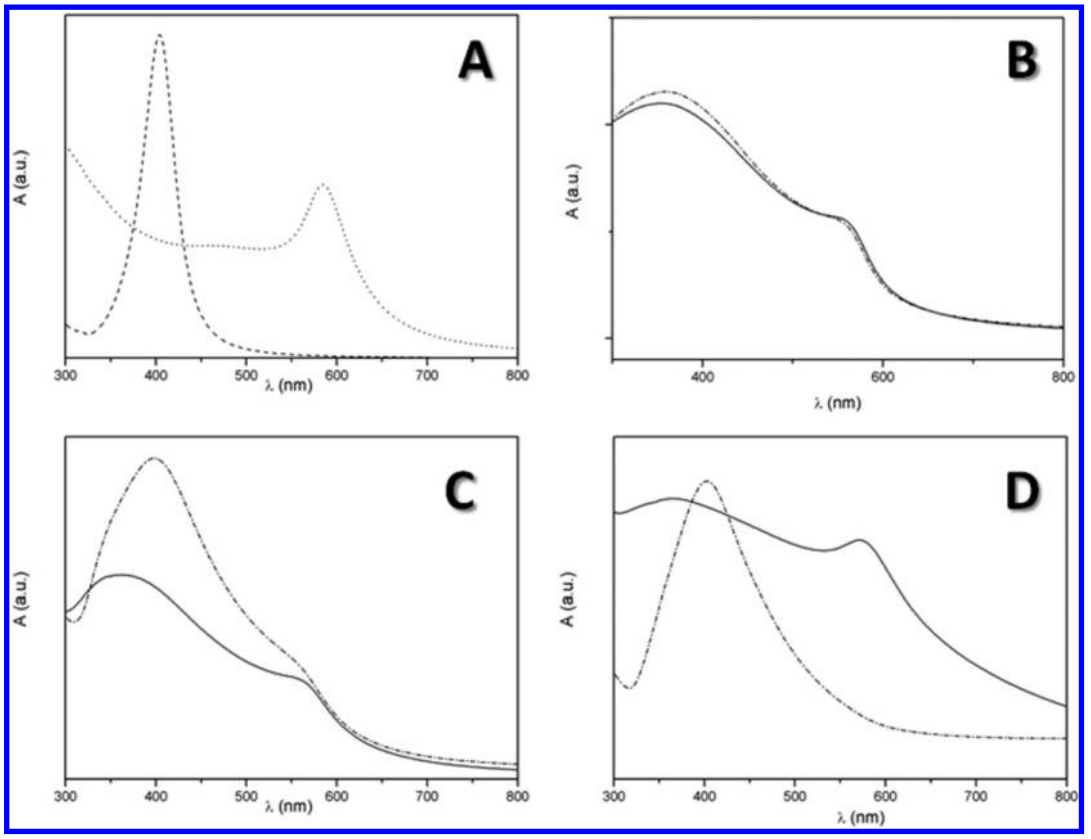

Figure 9. Optical spectrum of Cu (dotted line) and Ag (dashed line) (A). $Cu_4@Ag_1$ (plain line), $Cu_1@Ag_1$ (dot-dashed line) colloidal dispersion: shell grown by galvanic displacement (B) and metal assisted nucleation (C). Ag overgrowth (D).

± 1.6 nm. No sign of aging has been noticed on samples grown in these conditions. Dark-field image confirm the bimetallic nature of the particles. Figure 8C is a HRTEM showing some typical $Cu_1@Ag_1$. In this micrograph the crystalline nanospheres display well-resolved lattice-fringe contrast, and their identification was based on the analysis of this high-resolution image. Inset (a) represents the computed fast Fourier transform (FFT) of the portion of the image outlined by the white square and looks like a diffraction pattern, geometrically identical to that which would be recorded in a diffraction experiment. Analysis of this pattern revealed sets of reflections that could be readily referred to the cubic FCC structure of the elemental Ag (JCPDS 04-0783, a = 4.090 Å). Inset b represents the filtered and magnified portion of the image outlined by the white square. The distances measured between the lattice-fringes were 0.24 and 0.20 nm matching the interplanar spacing of d_{111} and d_{200} family of planes in the above-mentioned cubic structure of Ag. In this manner, using FFT from the region of the image (white square) in Figure 8C, it was possible to identify unambiguously the Ag crystalline shell coating the Cu.

Localized Surface Plasmon Resonance (LPSR). Optical spectrum of Cu colloidal dispersion in hexane shows a broad band at λ = 585 nm corresponding to the localized surface plasmon resonance (LSPR) of Cu (Figure 9A). Cu NPs typically exhibit LSPR at around 600 nm.[19] Ag colloidal dispersion shows a broad band at λ = 400 nm corresponding to the LSPR of Ag. Cu@Ag colloidal dispersion displays two bands corresponding to the LPSR of Cu and Ag; the Cu band is shifted to higher energy as expected from the difference in plasma resonance frequencies (higher value for Ag compared to Cu).[20]

$Cu_4@Ag_1$ and $Cu_1@Ag_1$ with Ag shell grown by galvanic displacement have a maximum in absorption at λ = 558 nm (LSPR of Cu) and λ = 365 nm (LSPR of Ag) (Figure 9B). $Cu_4@Ag_1$ and $Cu_1@Ag_1$ with Ag shell grown by metal assisted nucleation have a maximum in absorption at λ = 560 nm (LSPR of Cu) and at λ = 370 and 398 nm, respectively (LSPR of Ag) (Figure 9C). $Cu_4@Ag_1$ with Ag shell overgrowth have a maximum in absorption at λ = 570 nm (LSPR of Cu) and at λ = 370 nm. $Cu_1@Ag_1$ displays only one band at λ = 402 nm (LSPR of Ag) (Figure 9D).

DISCUSSION

Cu@Ag Bimetallic Nanoparticles. Core−shell structure are very appealing, especially with a cheap core and an expensive shell materials. In the case of Cu@Ag, the motivation is obviously to pave the way toward conductive inks. Cu@Ag synthesis in organic solution by a two-step reaction of $Cu(acac)_2(OAm)_2$ and $Ag(OAm)^+$ complexes offers a way to use two reduction processes: galvanic displacement and amine reduction. Galvanic displacement is limited to the first layer if one assumes the formation of Ag monolayer on Cu. When the reaction is performed through galvanic displacement only, while combining data from EDS, DLS, TEM, and UV−vis spectrophotometer, the increase of Ag(I) concentration above a 4/1 Cu/Ag ratio has no effect on the particle size, the atomic ratio Cu/Ag, and LPSR band wavelength. Therefore, the reaction is self-limited by the surface (11% of the atoms for a 12 nm Cu NP). Since the reaction proceeds through the following equation $Cu_{(s)} + 2Ag^+_{(sol)} \rightarrow Cu^{2+}_{(sol)} + 2Ag_{(s)}$, a simple calculation for 12 nm Cu NPs of the expected Cu/Ag ratio

dx.doi.org/10.1021/jp3109545 | J. Phys. Chem. C 2013, 117, 3093−3100

gives a 4/1 value in very good adequation with the observed results.

Using higher temperature allows increasing the Ag shell by using OAm as a reducing agent through the oxidation of amine; this redox process only occurs above 120 °C in the time scale of the experiment. Since galvanic displacement is done in a first step, followed by thermal activation of the reaction, the Ag shell preferentially grows on top of Cu@Ag NPs and self-nucleation is not observed. Cu@Ag seeds Ag growth and activates the thermal decomposition of $Ag(OAm)^+$ complex. This growth process yields homogeneous Cu@Ag NPs with a controlled composition and size. Optical spectra LPSR show the variation of the two LPSR bands attributed to Ag (360−400 nm) and Cu (560−585 nm) as a function of Ag shell thickness.[1] Ag growth enhances the Ag LPSR band intensity which is also red-shifted from 360 to 400 nm, revealing the monolayer to multilayers growth. At higher temperature (>120 °C), Cu LPSR vanishes in $Cu_1@Ag_1$ while Ag LPSR is enhanced, which could be ascribed to a thicker layer of Ag masking the Cu core. In all cases, TEM and HRTEM show faceted monodisperse nanocrystals after several days or weeks.

Metastability of the Ag Shell. Nevertheless, the most striking result concerns the aging process of the particles observed from TEM, HRTEM, and DLS analyses. The stability of bimetallic system is crucial toward application and raises several fundamental considerations. As depicted in Figures 5 and 7A, Cu@Ag with Ag shell grown through galvanic displacement displays dewetting of Ag after several months in colloidal dispersion. The same effect is observed for Ag shell overgrown at higher temperature. TEM and DLS analyses are summarized in a schema (Figure 10) showing the different

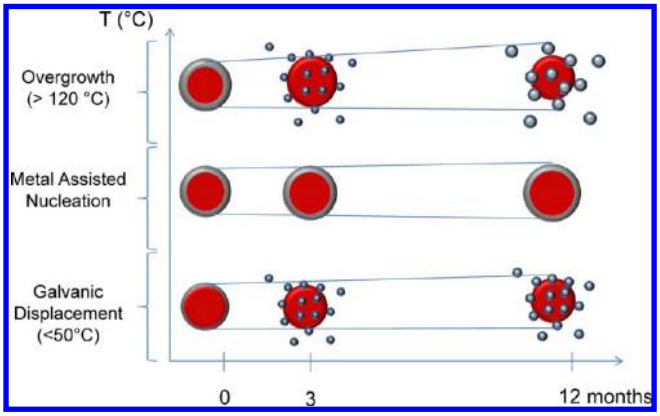

Figure 10. Schema of aging processes for different temperature ranges of Ag shell growth.

aging processes according to the Ag growth modes. The aging results in the formation of spherical Ag NPs on top of Cu NPs coated with OAm which is always in excess even after careful washings. Formation of directed heterostructure has been reported using a noble-metal-induced reduction process (NMIR)[21,22] or by a two-step reaction (Pt−Au).[23] In both cases, the anisotropy of the heterostructure arises from the lattice mismatch between the two metals. The bimetallic system decreases the interfacial energy by promoting the complete phase segregation.

According to our results, the nondirected segregation can occur from aging of pristine Cu@Ag NPs at room temperature. Ag crystallizes in the same space group as Cu but displays a lattice mismatch of 11.7%. This value seems too large for the system to accommodate, and Ag tends to recover a spherical shape while minimizing its interface with Cu (Figure 6B,C: HRTEM of Ag NPs on Cu). This phenomenon is also established when the Ag shell is overgrown at higher temperature (>120 °C) while metallic interdiffusion is more likely to occur. Thermodynamic stability of Cu@Ag in vacuum has already been investigated through molecular dynamics simulation on 1−10 nm NPs.[24] From these calculations, Ag−Cu solid solutions and Cu@Ag core−shell structure display the lowest stability for 2−10 nm NPs. On the contrary, Janus-like and Ag@Cu should be more stable. Using Monte Carlo simulations, surface segregation of Ag on Cu has been also established, Ag dewetting being a spontaneous phenomenon.[25] On the other hand, the colloids are dispersed in the presence of a long chain amine, and this surfactant could also have an influence on the shell rearrangement.[26] Recent theoretical and experimental work has pointed out the adsorption induced segregation in the Cu−Au system by Schiffrin et al.[27]

Our system Cu@Ag is a nice case study where metastable shell evolves spontaneously to Ag NPs at the surface. DLS shows unambiguously the growth process which combines the well-established Ostwald ripening of Cu and Ag NPs[28] once the dewetting process has been achieved. Obviously, the amine ligand is playing a role as already observed with Au−Cu NPs where atomic diffusion is inhibited by the presence of amines.[29] Ag−Cu system differs from Au−Cu (and Cu−Pd[30] or Cu−Pt[31] alloys) from a thermodynamic consideration since the two metals do not form alloy in the bulk. Based on these other systems, surface energy is widely modified by the chemical affinity of chemisorbed molecules, here amines, with metallic atoms. Ag would then segregate to maximize the metallic surface, both Ag and Cu, exposed to the ligands.

From a more applied viewpoint, Cu@Ag stands as a good candidate for printing electronics. Some recent reports have stressed the role of Ag migration in Cu@Ag thin films after sintering beyond 250 °C on submicronic grains.[32] The reported enhanced conductivity values have been linked to the Ag interconnections between Cu grains. Our work supports the formation of Ag grains at the nanoscale even at room temperature. On the other hand, a slight change in the temperature growth of Ag shell (75 °C) gives a stable Cu@Ag core/shell after 3 months (Figures 7 and 8) to more than 1 year. As stated above, the main driving force to metallic segregation stands in the lattice mismatch between Ag and Cu. Since temperature increase results in interdiffusion of Ag and Cu at the interface between core and shell, the enhanced stability probably results from the optimized roughness of the interface. The role of the ligand shell has certainly not do be downplayed and is the focus of further investigation while studying the ligand exchange influence on the Cu@Ag stability. The temperature window proposed for the stability has also to be rationalized by a model supporting the experimental data.

■ CONCLUSIONS

Cu and Cu@Ag monodisperse NPs have been synthesized using a solvothermal route based on oleylamine (OAm) complexes. Ag shell growth has been followed by HRTEM and DLS, proceeding from galvanic displacement in organic solution to form an Ag monolayer in average as demonstrated from EPR and EDS. Further growth results from temperature-induced OAm-based reduction assisted by the metallic nanoparticle. Ag shell stability has been studied by HRTEM and DLS. Aging over 1 year shows dewetting of Ag on Cu to

dx.doi.org/10.1021/jp3109545 | J. Phys. Chem. C 2013, 117, 3093−3100

yield Ag NPs attached to the Cu surface. The further aging removes the Ag NPs from the surface, OAm excess stabilizing the newly formed NPs. This atomic rearrangement has been theoretically predicted for small bimetallic NPs starting from Cu/Ag alloys or Cu@Ag. Calculations always show the unstability of Cu@Ag arrangement due to the interfacial stress. On the other hand, we have succeeded in the stabilization of Cu@Ag configuration by controlling the temperature of Ag growth. The phenomenon is very significant for printed electronics where Ag migration by sintering enhances the conductivity. This phenomenon is demonstrated in a comprehensive way for nanoscale particles in the present work.

AUTHOR INFORMATION

Corresponding Author

*E-mail david.zitoun@biu.ac.il.

Notes

The authors declare no competing financial interest.

REFERENCES

(1) Ferrando, R.; Jellinek, J.; Johnston, R. L. *Chem. Rev.* **2008**, *108*, 845−910.
(2) Wang, D.; Li, Y. *Adv. Mater.* **2011**, *23*, 1044−1060.
(3) Cortie, M. B.; McDonagh, A. M. *Chem. Rev.* **2011**, *111*, 3713−3735.
(4) Sobal, N. S.; Hilgendorff, M.; Mo, H.; Giersig, M.; Spasova, M.; Radetic, T.; Farle, M. *Nano Lett.* **2002**, *2*, 621−624.
(5) Lu, X.; Au, L.; McLellan, J.; Li, Z.-Y.; Marquez, M.; Xia, Y. *Nano Lett.* **2007**, *7*, 1764−1769.
(6) Lee, W.-R.; Kim, M. G.; Choi, J.-R.; Park, J.-I.; Ko, S. J.; Oh, S. J.; Cheon, J. *J. Am. Chem. Soc.* **2005**, *127*, 16090−16097.
(7) Park, J.; Joo, J.; Kwon, S. G.; Jang, Y.; Hyeon, T. *Angew. Chem., Int. Ed.* **2007**, *46*, 4630−4660.
(8) Zhang, J.; Tang, Y.; Weng, L.; Ouyang, M. *Nano Lett.* **2009**, *9*, 4061−4065.
(9) Cazayous, M.; Langlois, C.; Oikawa, T.; Ricolleau, C.; Sacuto, A. *Phys. Rev. B* **2006**, *73*, 113402.
(10) Grouchko, M.; Kamyshny, A.; Magdassi, S. *J. Mater. Chem.* **2009**, *19*, 3057.
(11) Zhang, J.; Yuan, Y.; Xu, X.; Wang, X.; Yang, X. *ACS Appl. Mater. Interfaces* **2011**, *3*, 4092−4100.
(12) Chen, L. Y.; Zhang, L.; Fujita, T.; Chen, M. W. *J. Phys. Chem. C* **2009**, *113*, 14195−14199.
(13) Tsuji, M.; Hikino, S.; Sano, Y.; Horigome, M. *Chem. Lett.* **2009**, *38*, 518−519.
(14) Tsuji, M.; Hikino, S.; Tanabe, R.; Yamaguchi, D. *Chem. Lett.* **2010**, *39*, 334−336.
(15) Gonzalez, E.; Arbiol, J.; Puntes, V. F. *Science* **2011**, *334*, 1377−1380.
(16) Uk Son, S.; Kyu Park, I.; Park, J.; Hyeon, T. *Chem. Commun.* **2004**, *1*, 778−779.
(17) Cho, Y.; Huh, Y. *Mater. Lett.* **2009**, *63*, 227−229.
(18) Hung, L.-I.; Tsung, C.-K.; Huang, W.; Yang, P. *Adv. Mater.* **2010**, *22*, 1910−1914.
(19) Wei, Y.; Chen, S.; Kowalczyk, B.; Huda, S.; Gray, T. P.; Grzybowski, B. A. *J. Phys. Chem. C* **2010**, *114*, 15612−15616.
(20) Mulvaney, P. In *Nanoscale Materials in Chemistry*; Klabunde, K., Ed.; Wiley: New York, 2001.
(21) Wang, D. S.; Li, Y. D. *J. Am. Chem. Soc.* **2010**, *132*, 6280−6281.
(22) Wang, D. S.; Peng, Q.; Li, Y. D. *Nano Res.* **2010**, *3*, 574−580.
(23) Habas, S. E.; Lee, H.; Radmilovic, V.; Somorjai, G. A.; Yang, P. *Nat. Mater.* **2007**, *6*, 692−697.
(24) Delogu, F. *J. Phys. Chem.C* **2010**, *114*, 19946−19951.
(25) Lequien, F.; Creuze, J.; Berthier, F.; Braems, I.; Legrand, B. *Phys. Rev. B* **2008**, *78*, 075414.
(26) Feng, Y.; He, J.; Wang, H.; Tay, Y. Y.; Sun, H.; Zhu, L.; Chen, H. *J. Am. Chem. Soc.* **2012**, *134*, 2004−2007.
(27) Völker, E.; Williams, F. J.; Calvo, E. J.; Jacob, T.; Schiffrin, D. J. *Phys. Chem. Chem. Phys.* **2012**, *14*, 7448−7455.
(28) Smetana, A. B.; Klabunde, K. J.; Sorensen, C. M.; Ponce, A. A.; Mwale, B. *J. Phys. Chem. B* **2006**, *110*, 2155−2158.
(29) Dilshad, N.; Ansari, M. S.; Beamson, G.; Schiffrin, D. J. *J. Mater. Chem.* **2012**, *22*, 10514−10524.
(30) Jirkovský, J. S.; Panas, I.; Romani, S.; Ahlberg, E.; Schiffrin, D. J. *J. Phys. Chem. Lett.* **2012**, *3*, 315−321.
(31) Mayrhofer, K. J. J.; Hartl, K.; Juhart, V.; Arenz, M. *J. Am. Chem. Soc.* **2009**, *131*, 16348−16349.
(32) Kim, S. J.; Stach, E. A.; Handwerker, C. A. *Appl. Phys. Lett.* **2010**, *96*, 144101.